

Numerical evolutions of the linearised conformal Einstein field equations in the inversion-Minkowski spacetime

Christian Peterson  ^{*}1, Edgar Gasperín  [†]1, and Alex Vañó-Viñuales  [‡]1

¹ *CENTRA, Departamento de Física, Instituto Superior Técnico IST, Universidade de Lisboa UL, Avenida Rovisco Pais 1, 1049 Lisboa, Portugal*

12th March 2025

Abstract

Numerical evolutions of a system of equations close to null infinity in the geometric background of the *inversion-Minkowski spacetime* are performed. The evolved equations correspond to the linearisation of a second order metric formulation of the conformal Einstein field equations (CEFEs). These linear equations were first presented in [1] and the main purpose of this paper is to illustrate, through numerical evolutions, the scri-fixing technique via gauge source functions introduced [1] for the linearised CEFEs. A comparison of evolutions using scri-fixing gauge sources and trivial gauge source function in spherical and axial symmetry is presented.

Keywords: conformal boundary, conformal Einstein field equations, scri-fixing.

1 Introduction

The original notion of gravitational waves can be traced back to the linearisation of the Einstein field equations and the well-known quadrupole formula—for a historical overview see [2, 3]. However, it took several decades for a complete understanding gravitational radiation at the non-linear level to be achieved [4, 5, 6]. The reason is that the non-linear notion of gravitational radiation requires to be able to evaluate certain quantities at null-infinity \mathcal{I} [7, 8, 9, 10]—the mathematical idealisation of the asymptotic region of spacetime. In turn, \mathcal{I} is formally defined not at the level of the physical spacetime $(\tilde{\mathcal{M}}, \tilde{g})$ but rather through a conformally related manifold with metric (\mathcal{M}, g) where $g = \Xi^2 \tilde{g}$ which we call *unphysical spacetime*—see [11] for the origin of this terminology. Then, \mathcal{I} is identified with the points in \mathcal{M} for which $\Xi = 0$ but $d\Xi \neq 0$. Given that the Einstein field equations are not conformally invariant obtaining an initial value formulation that includes \mathcal{I} is not trivial. Yet, nowadays there are different proposals to include \mathcal{I} in the initial value formulation of general relativity. One can classify some of these proposals by analysing how the conformal factor Ξ is treated. The first approach is to take Ξ —or some other boundary-defining function—as a non-dynamical quantity and evolve the unphysical metric g —or other equivalent set of rescaled variables—using hyperboloidal foliations. Some examples of formulations of the Einstein field equations where this approach is followed are [12, 13, 14, 15, 16] and, although they are different in several important details they share essentially the core idea described above and we will refer to them as the *formally singular hyperboloidal approach*. Its

^{*}E-mail address: christian.peterson@tecnico.ulisboa.pt

[†]E-mail address: edgar.gasperin@tecnico.ulisboa.pt

[‡]E-mail address: alex.vano.vinuales@tecnico.ulisboa.pt

most evident advantage is that it allows to set up the Einstein equations for hyperboloidal evolution in a way similar to current Numerical Relativity simulations of merging binaries targeting astrophysical applications. Another positive point is that the prescribed conformal factor Ξ allows to set the location of \mathcal{S} at a fixed coordinate location (usually the outer boundary of the domain). The second approach to the inclusion of \mathcal{S} is to consider Ξ as a dynamical quantity, with its evolution governed directly by the Einstein field equations. Promoting Ξ to the level of an evolved field forces one to introduce the curvature as a further unknown which then results in a set of equations, which although equivalent to the Einstein field equations when $\Xi = 1$, look very different to standard formulations of general relativity. Following this general strategy one arrives at the *conformal Einstein field equations* (CEFEs) originally introduced in [17] by H. Friedrich—see [18] for a comprehensive discussion. The basic advantage of the CEFEs is that, in contrast with the formally singular hyperboloidal approach, they are *formally regular* in the sense that Ξ^{-1} terms do not appear in the equations. Despite the fact that there are already a number of numerical and mathematical results obtained with the CEFEs [17, 19, 20, 21, 22, 23, 24, 25, 26] in general, they remain to some extent relatively unexploited for physical applications as compared with other more standard formulations. Given that the linearisation of the Einstein field equations has been the starting point of several important areas aimed to astrophysical applications such as the self-force program, quasinormal modes and black hole spectroscopy, it is natural to pursue analogous calculations using the CEFEs to evaluate quantities of physical interest at \mathcal{S} . Furthermore, the relevance of the inclusion of \mathcal{S} in these calculations is evidenced by the success of the hyperboloidal approach for linear perturbation theory [27, 28, 29, 30, 31]. A fundamental difference between the hyperboloidal approach in the study of linear equations and that of the non-linear equations is that in the former case the equations are regular while in the latter case, formally singular. Nevertheless, numerical evidence suggest that these formally singular terms (composed of divergent factors multiplied by fields that decay implicitly) in fact acquire finite limits. Hence, with these motivations, in [1] the CEFEs were linearised using a particular form that is closer to traditional formulations of the Einstein field equations used in Numerical Relativity: wave equations with gauge source functions (generalised harmonic gauge). Therefore, [1] represents the linear version of the non-linear formulation [32, 33] which seems to be the hyperbolic reduction of the CEFEs which more closely resembles standard formulations used in Numerical Relativity. One of the lessons learned in [1] is that, at least at the linear level, the freedom in the gauge source functions can be used to fix the conformal factor Ξ in an, essentially, ad-hoc way. A similar scri-fixing through gauge source functions in the non-linear case would open the possibility of using the coordinates and gauges well understood in the formally singular hyperboloidal approach [13, 14, 34, 30] but with the formally regular equations that the CEFEs provide. Whether this is in fact possible, and its relation to Zenginoğlu’s scri-fixing [35, 12] and Frauendiener’s scri-freezing shift gauges [36] will be explored elsewhere. To test these ideas numerically in a relatively simple arena, in this paper we perform numerical evolutions of the linearised metric and second order CEFEs derived in [1].

2 Geometric set-up and formulation

Although the purpose of this article is to perform numerical evolutions of the linearised CEFEs presented in [1], to have an abridged but self-contained discussion, in this section we briefly revisit the non-linear CEFEs and its linearisation.

2.1 The conformal Einstein field equations

The conformal Einstein field equations (CEFEs) were originally introduced in 1981 in [17]. This reformulation of the Einstein field equations is based on Penrose’s idea of conformal compactification in which $(\tilde{\mathcal{M}}, \tilde{g})$ is the physical spacetime that satisfies the Einstein field equations and

one considers a conformally related manifold with metric $(\mathcal{M}, \mathbf{g}, \Xi)$ where $\mathbf{g} = \Xi^2 \tilde{\mathbf{g}}$ that is called the unphysical spacetime. If the physical spacetime satisfies the vacuum Einstein field equations $\tilde{R}_{ab} = \lambda \tilde{g}_{ab}$ then the CEFEs read

$$\nabla_a \nabla_b \Xi + \Xi L_{ab} - s g_{ab} = 0, \quad (1a)$$

$$\nabla_a s + L_{ac} \nabla^c \Xi = 0, \quad (1b)$$

$$\nabla_a L_{bc} - \nabla_b L_{ac} - d^d{}_{cab} \nabla_d \Xi = 0, \quad (1c)$$

$$\nabla_e d^e{}_{abc} = 0, \quad (1d)$$

$$R^c{}_{dab} - \Xi d^c{}_{dab} - 2(\delta^c{}_{[a} L_{b]d} - g_{d[a} L_{b]}{}^c) = 0. \quad (1e)$$

$$\lambda - 6\Xi s + 3\nabla_a \Xi \nabla^a \Xi = 0 \quad (1f)$$

where Ξ is the conformal factor, L_{ab} is the Schouten tensor, d_{abcd} is the rescaled Weyl tensor and s is the Friedrich scalar, defined in terms of more familiar quantities via

$$s := \frac{1}{4} \nabla_a \nabla^a \Xi + \frac{1}{24} R \Xi, \quad (2)$$

$$L_{ab} := \frac{1}{2} R_{ab} - \frac{1}{12} R g_{ab}, \quad (3)$$

$$d^a{}_{bcd} := \Xi^{-1} C^a{}_{bcd}. \quad (4)$$

where $C^a{}_{bcd}$, $R^a{}_{bcd}$, R_{ab} and R are the Weyl, Riemann, Ricci tensor and Ricci scalar of \mathbf{g} .

The CEFEs as written above can be thought as merely a set of identities satisfied by the curvature tensors and other geometric objects defined on $(\mathcal{M}, \mathbf{g})$. The process of recasting the standard Einstein field equations (or the CEFEs given above) as a set of partial differential equations is called a hyperbolic reduction since the equations are split into evolution and constraint equations, being the former of hyperbolic type. The CEFEs are *formally* regular in the sense that there are no Ξ^{-1} terms in equations (1). There are different hyperbolic reduction strategies for the CEFEs and the one that we are interested in, is the metric and second order hyperbolic reduction of the CEFEs first introduced in [33] —see [32] for the case where trace-free matter is included. An appealing property of this hyperbolic reduction is that the metric satisfies a set of wave equations which looks formally identical to the *standard* Einstein field equations in *generalised harmonic gauge* —which fixes the gauge through (coordinate) gauge source functions H^a — used in Numerical Relativity, with the addition of a few extra terms. These extra terms are related to the fields Ξ , s , L_{ab} and d_{abcd} which can be thought as some “geometric-artificial-matter” which, in turn, satisfy another set of wave equations. In fact, in this formulation is convenient to use the trace-free Ricci tensor $\Phi_{ab} := \frac{1}{2}(R_{ab} - \frac{1}{4}Rg_{ab})$ instead of L_{ab} as an evolved variable. This is because in the CEFEs the Ricci scalar R is related to the choice of conformal representative and hence is called the conformal gauge source function F . See [32] and [1] for further details.

Note that, despite their mathematically appealing properties for the inclusion of \mathcal{I} in the numerical domain, the constraint subsystem of the CEFEs is larger than in most common approaches. Therefore, they pose an additional difficulty when one is to think about numerical simulations of systems of physical interest, mainly because the constraints will be unavoidably violated due to numerical error. Whether constraint violations remain bounded in free evolution schemes will be studied elsewhere. In this work we focus in the evolution sector of the linearised CEFEs in order to test the scri-fixing technique of [1], which is independent of the initial data used for evolutions.

2.2 The linearised conformal Einstein field equations in second order form

In [1] the linearisation of the second order formulation of the CEFEs of [32] was presented. These equations were derived for any background and they will only be presented schematically here.

At the end of this section we fix our attention to conformally flat backgrounds and write the equations explicitly.

Let φ encode all the geometric variables while \mathbf{f} encodes the gauge quantities. To linearise the second order metric formulation of the CEFs one starts by considering the split:

$$g_{ab} = \mathring{g}_{ab} + \delta g_{ab}, \quad \Phi_{ab} = \mathring{\Phi}_{ab} + \delta \Phi_{ab}, \quad \Xi = \mathring{\Xi} + \delta \Xi, \quad s = \mathring{s} + \delta s \quad (5)$$

where the ring-quantities represent an exact (background) solution to the CEFs and the delta-quantities are perturbations. The term \mathbf{f} encodes the *Lorenz gauge source functions* F^a —related to the linearisation of the coordinate gauge source functions δH^a — and the perturbation of the conformal gauge source function δF —see [1] for further details. With this notation, the linearised second order CEFs read

$$\begin{aligned} \mathring{\square} \delta g_{ab} &= H_{(ab)}^g(\delta \varphi, \mathring{\nabla} \delta \varphi; \mathring{\varphi}, \mathbf{f}, \mathring{\nabla} \mathring{\varphi}, \mathring{\nabla} \mathbf{f}) \\ \mathring{\square} \delta \Xi &= H^\Xi(\delta \phi, \mathring{\nabla} \delta \phi; \mathring{\varphi}, \mathbf{f}, \mathring{\nabla} \mathring{\varphi}) \\ \mathring{\square} \delta s &= H^s(\delta \varphi, \mathring{\nabla} \delta \varphi; \mathring{\varphi}, \mathbf{f}, \mathring{\nabla} \mathring{\varphi}, \mathring{\nabla} \mathbf{f}) \\ \mathring{\square} \delta \Phi_{ab} &= H_{(ab)}^\Phi(\delta \varphi, \mathring{\nabla} \delta \varphi; \mathring{\varphi}, \mathbf{f}, \mathring{\nabla} \mathring{\varphi}, \mathring{\nabla} \mathbf{f}, \mathring{\nabla} \mathring{\nabla} F, \mathring{\nabla} \mathring{\nabla} \delta F) \\ \mathring{\square} \delta d_{abcd} &= H_{[ab][cd]}^d(\delta \varphi, \mathring{\nabla} \delta \varphi; \mathring{\varphi}, \mathbf{f}, \mathring{\nabla} \mathring{\varphi}, \mathring{\nabla} \mathring{\nabla} \mathring{\varphi}, \mathring{\nabla} \mathring{\nabla} \mathbf{f}). \end{aligned} \quad (6)$$

Here $\mathring{\square} := \mathring{g}^{ab} \mathring{\nabla}_a \mathring{\nabla}_b$ where $\mathring{\nabla}$ denotes the Levi-Civita connection of \mathring{g} . Observe that the semicolon separates the arguments which do not contain the evolved perturbation variables. Notice that only the equation for $\delta \Phi_{\mu\nu}$ contains second derivatives of δF which restricts the allowed choices for δF .

3 The background unphysical spacetime and scri-fixing

In this section the geometry of the conformal background is discussed as well as the scri-fixing strategy via gauge source functions for the linearised CEFs of [1].

3.1 The inversion-Minkowski spacetime

The (physical) Minkowski spacetime metric in spherical polar coordinates reads

$$\tilde{\eta} = -d\tilde{t} \otimes d\tilde{t} + d\tilde{r} \otimes d\tilde{r} + \tilde{r}^2 \boldsymbol{\sigma}, \quad (7)$$

with $\tilde{t} \in (-\infty, \infty)$, $\tilde{r} \in [0, \infty)$ where $\boldsymbol{\sigma}$ denotes the standard metric on \mathbb{S}^2 . Recall that for any conformally flat metric $\mathbf{g} = \Xi^2 \tilde{\eta}$ in general one has:

$$\Phi_{ab} \neq 0, \quad R \neq 0, \quad d_{abcd} = 0. \quad (8)$$

However, there exist a non-trivial rescaling ($\Xi \neq \text{const}$) for which the unphysical metric \mathbf{g} is again flat. This is a classical conformal representation of Minkowski that can be consulted in [37]. To see this explicitly, one introduces unphysical coordinates (t, r) given by:

$$t = \frac{\tilde{t}}{\tilde{r}^2 - \tilde{t}^2}, \quad r = \frac{\tilde{r}}{\tilde{r}^2 - \tilde{t}^2}. \quad (9)$$

A direct calculation then shows that

$$\boldsymbol{\eta} = \Xi^2 \tilde{\eta} \quad (10)$$

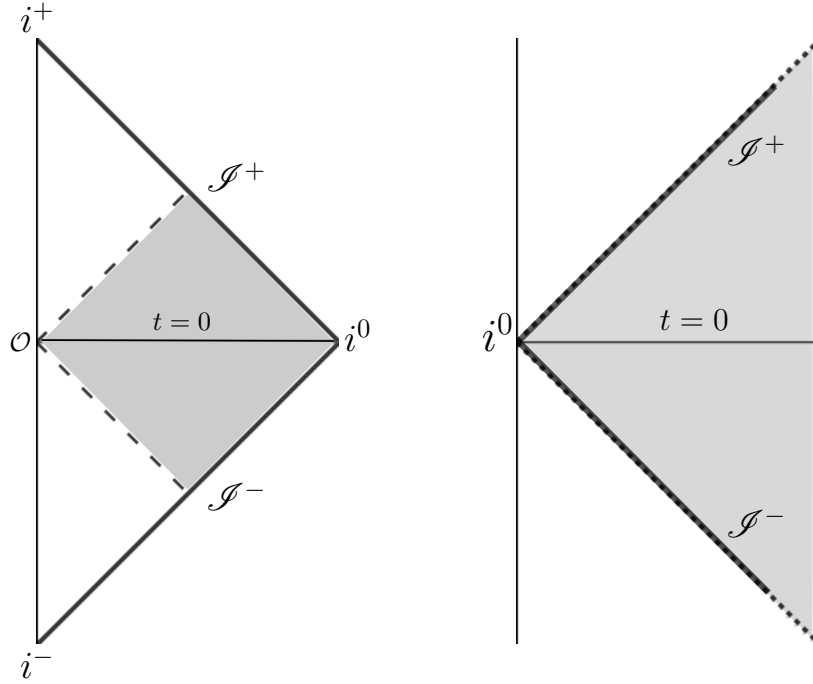


Figure 1: The left panel shows the Penrose diagram of the Minkowski spacetime where the shaded region corresponds to that covered by the *inversion conformal representation*. As depicted in the right panel, in the inversion-Minkowski spacetime, \mathcal{I}^\pm is represented by the lightcone through the unphysical origin which, in turn, corresponds to i^0 .

where

$$\eta = -dt \otimes dt + dr \otimes dr + r^2 \sigma, \quad \Xi = r^2 - t^2. \quad (11)$$

One can verify that the associated Friedrich scalar is constant $s = 2$. We call this conformal representation the *inversion-Minkowski* spacetime since the roles of spatial infinity i^0 and the physical origin \mathcal{O} are swapped. Hence, in the unphysical picture future and past null infinity \mathcal{I}^\pm correspond to the lightcone through the unphysical origin. Therefore, the inversion-Minkowski spacetime is not a full compactification of the physical spacetime in the sense that \mathcal{O} is located at $r \rightarrow \infty$ and the future and past timelike infinities i^\pm are also not included in the domain. Despite this drawback notice that one can still have access to a portion of \mathcal{I}^\pm —see diagram 1. Naturally, one could opt to choose another conformal compactification of the Minkowski spacetime such as the one that conformally embeds the Minkowski spacetime into the Einstein cylinder (used for instance to obtain the textbook Penrose diagrams of Minkowski, de Sitter and anti-de Sitter spacetimes) so that one has a full compactification of the spacetime. This is of particular interest, but comes with the price that $\Phi_{ab} \neq 0$ and $R \neq 0$, which renders most of the linearised equations (6) (except that for the equation for the perturbation of the Weyl tensor) excessively long and cumbersome to deal with. Hence, the inversion-Minkowski spacetime is chosen for its simplicity and clean implementation but from the formulation point of view one could have equally opted for an analogous implementation in the Einstein’s cylinder background.

3.2 The linearised CEFs around a flat background

In this section we write the linearised second order metric CEFs for the particular case in which \hat{g} is flat, this achieved non-trivially only in the case of the inversion conformal representation

of the Minkowski spacetime as discussed in the previous section. In this case the background quantities read

$$\overset{\circ}{\Phi}_{ab} = \overset{\circ}{R} = \overset{\circ}{d}_{abcd} = 0, \quad \overset{\circ}{\Xi} = r^2 - t^2, \quad \overset{\circ}{s} = 2. \quad (12)$$

This is the case for which the general expression simplify the most and they explicitly read:

$$\overset{\circ}{\square}\delta g_{\mu\nu} = -4\delta\Phi_{\mu\nu} - \overset{\circ}{g}_{\mu\nu}\overset{\circ}{\nabla}_\alpha F^\alpha + 2\overset{\circ}{\nabla}_{(\mu}F_{\nu)} + \frac{1}{2}\mathcal{F}\overset{\circ}{g}_{\mu\nu}, \quad (13a)$$

$$\overset{\circ}{\square}\delta\Xi = 4\delta s - \overset{\circ}{s}\delta g^\mu{}_\mu + F^\mu\overset{\circ}{\nabla}_\mu\overset{\circ}{\Xi} - \frac{1}{6}\overset{\circ}{\Xi}\mathcal{F}, \quad (13b)$$

$$\overset{\circ}{\square}\delta s = -\frac{1}{6}\overset{\circ}{s}\mathcal{F} - \frac{1}{6}\overset{\circ}{\nabla}_\mu\mathcal{F}\overset{\circ}{\nabla}^\mu\overset{\circ}{\Xi}, \quad (13c)$$

$$\overset{\circ}{\square}\delta\Phi_{\mu\nu} = \frac{1}{6}\overset{\circ}{\nabla}_{\{\mu}\overset{\circ}{\nabla}_{\nu\}}\mathcal{F}, \quad (13d)$$

$$\overset{\circ}{\square}\delta d_{\mu\nu\alpha\beta} = 0. \quad (13e)$$

here parenthesis represent symmetrisation while curly brackets denote taking the symmetric trace-free part. Also, to simplify the notation we have denoted δF by \mathcal{F} so that only perturbation evolved quantities have a δ decoration.

3.3 Gauge sources and scri-fixing strategies

The linear analogue of the conformal and coordinate gauge source functions are encoded via \mathcal{F} and F^a , respectively. An advantageous property of the generalised harmonic gauge formulation is that one can leverage the choice of gauge source functions. For instance in hyperboloidal formulation of [38, 16] the gauge source functions are chosen to drive the asymptotic behaviour of the fields. In contrast, in the case of the CEFs current numerical and analytical studies make use of the so-called conformal Gaussian gauge [25, 39, 26, 20]. Although the conformal Gaussian gauge is a very geometrical choice for which the conformal factor is not longer an unknown it comes with a price: the transformation connecting the “physical” and “unphysical” coordinates is not known explicitly but rather fixed through a set of ordinary differential equations (the conformal geodesic equations) which more often than not, cannot be solved in closed form. Even in the cases where these expressions can be reduced to quadratures it is not possible to write, in a simple and closed form way, physically important metrics such as that of the Schwarzschild or Kerr spacetimes — see for instance [40, 41]. This is in stark contrast with the hyperboloidal approach of [42, 43] where the change of coordinates from physical to unphysical coordinates and/or conformal factor is given in a well-motivated but essentially ad-hoc way. This is particularly advantageous as this allows to write most physically relevant spacetimes in hyperboloidal coordinates in an explicit and closed form — see for instance [44]. In [1] it was noticed that, at least for the linear case, one can leverage the gauge source functions to achieve a scri-fixing similar to that of the hyperboloidal approach but for the linearised CEFs. To do so, observe that one can allow F^a to be a function of the coordinates as well as the fields φ while \mathcal{F} can depend on the coordinates (but not φ) without breaking the hyperbolicity of these equations. Also notice that the zeros of the conformal factor Ξ do not necessarily coincide as those of the background conformal factor $\overset{\circ}{\Xi}$ as one has $\Xi = \overset{\circ}{\Xi} + \delta\Xi$. Hence, scri-fixing for the linear case simply means being able to ensure that $\delta\Xi = 0$ so that the zeros of the full conformal factor Ξ correspond to those of that of the background conformal factor $\overset{\circ}{\Xi}$. In the current linear set up one can achieve this scri-fixing by simply choosing $F^a(x; \varphi)$ such that

$$F^a\overset{\circ}{\nabla}_a\overset{\circ}{\Xi} = \frac{1}{6}\overset{\circ}{\Xi}\mathcal{F} - 4\delta s + \overset{\circ}{\Xi}\overset{\circ}{\Phi}^{ab}\delta g_{ab} + \overset{\circ}{s}\delta g^a{}_a. \quad (14)$$

Therefore $\overset{\circ}{\square}\delta\Xi = 0$. Hence, setting trivial initial data for $\delta\Xi$ in conjunction with existence and uniqueness of wave equations will ensure that $\delta\Xi = 0$. Notice however that, this method already

shows its limitations regarding the problem at i^0 since in order to solve for F^a in equation (14) one needs $\hat{\nabla}_a \hat{\Xi} \neq 0$. In other words, this gauge choice works for any slicing for which $\hat{\nabla}_a \hat{\Xi} \neq 0$ everywhere. A particular example of these slices are hyperboloidal slices as they precisely avoid the neighbourhood of i^0 . The scri-fixing method for the linearised CEFs of [1] is very similar in spirit to the scri-fixing technique introduced for the hyperboloidal approach in [35, 12]. Conceptually, the difference is that method is to be applied to a formally regular set of equations (CEFs) instead of a formally singular one. It should be pointed out, however, that there exist already in the CEFs literature a similar choice called the scri-freezing shift gauge [36]. Understanding the relation between these three gauge choices aimed to control the location of \mathcal{S} will be explored elsewhere.

4 Numerical implementation and results

In this section we describe the numerical implementation of the equations and the results of the numerical evolutions performed for this work.

4.1 3+1 decomposition

Although equations (13) are clearly hyperbolic —as long as $\mathcal{F} = \mathcal{F}(x^\mu)$ and $F^a = F^a(\phi, x^\mu)$ — for numerical purposes it is convenient to perform a 3+1 split of both the evolved fields and the background geometry. The customary 3+1 decomposition will not be repeated here and this section will simply serve to set up the notation and conventions for the subsequent discussion. The background spacetime metric is decomposed as $\hat{g}_{ab} = \hat{\gamma}_{ab} - \hat{n}_a \hat{n}_b$, where \hat{n} is the normal to some fiduciary spacelike hypersurface \mathcal{S} with induced metric γ . The extrinsic curvature \hat{K} , normal \hat{n} and acceleration vector \hat{a} are related via $\hat{\nabla}_a \hat{n}_b = \hat{K}_{ab} + \hat{a}_b \hat{n}_a$ where $\hat{a}^a = -\hat{n}^b \hat{\nabla}_b \hat{n}^a$. The tensorial perturbation variables are decomposed accordingly:

$$\begin{aligned} \delta g_{nn} &:= \hat{n}^a \hat{n}^b \delta g_{ab}, & \delta g_{na} &:= \hat{\gamma}_a^c \hat{n}^b \delta g_{cb}, & \delta \gamma_{ab} &:= \hat{\gamma}_a^c \hat{\gamma}_b^d \delta g_{cd}. \\ \delta \Phi_{nn} &:= \hat{n}^a \hat{n}^b \delta \Phi_{ab}, & \delta \Phi_{na} &:= \hat{\gamma}_a^c \hat{n}^b \delta \Phi_{cb}, & \delta \phi_{ab} &:= \hat{\gamma}_a^c \hat{\gamma}_b^d \delta \Phi_{cd} \\ \delta E_{ab} &:= \hat{n}^b \hat{n}^d \delta d_{abcd}, & \delta B_{ab} &:= \hat{n}^b \hat{n}^d \delta d_{abcd}^*. \end{aligned}$$

where $\delta d_{abcd}^* := \frac{1}{2} \hat{\epsilon}_{cd}^{pq} \delta d_{abpq}$ and $\hat{\epsilon}_{abcd}$ is the volume form of \hat{g} . Finally, the Lorenz source functions are decomposed as

$$F_n = \hat{n}^a F_a, \quad f_a = \hat{\gamma}_a^c F_c. \quad (15)$$

Since the numerical infrastructure we will use (NRPy+ [45], see the next subsection for more details) is built for first order in time and second order in space equations, in the final equations to be implemented we have introduced time-reduction-variables defined through the Lie derivative along \hat{n} . For instance we define the time reduction variable $\delta \phi_{ab}^\pi := \mathcal{L}_{\hat{n}} \delta \phi_{ab}$ and then use the wave equation (13d) to obtain a first order in time evolution equation for $\delta \phi_{ab}^\pi$. We proceed similarly with all the variables. The final form of the equations will not be displayed here. This calculation was carried out using `xAct` in `Mathematica`. Additionally, using equation (14) one obtains that, in this case, the gauge source functions that achieve the scri-fixing are those satisfying:

$$-tF_n + rf^r = -2\delta s + \frac{1}{12} \mathcal{F} r^2 - \frac{1}{2} \hat{s} \delta g_{nn} - \frac{1}{12} - \mathcal{F} t^2 \frac{1}{2} \hat{s} \hat{\gamma}^{ij} - \delta \gamma_{ij}. \quad (16)$$

For the numerical evolutions discussed in the next section two sets of gauge source functions will be used, one for which all the gauge source functions are zero and other for which all vanish except for F_n , which satisfies equation (16).

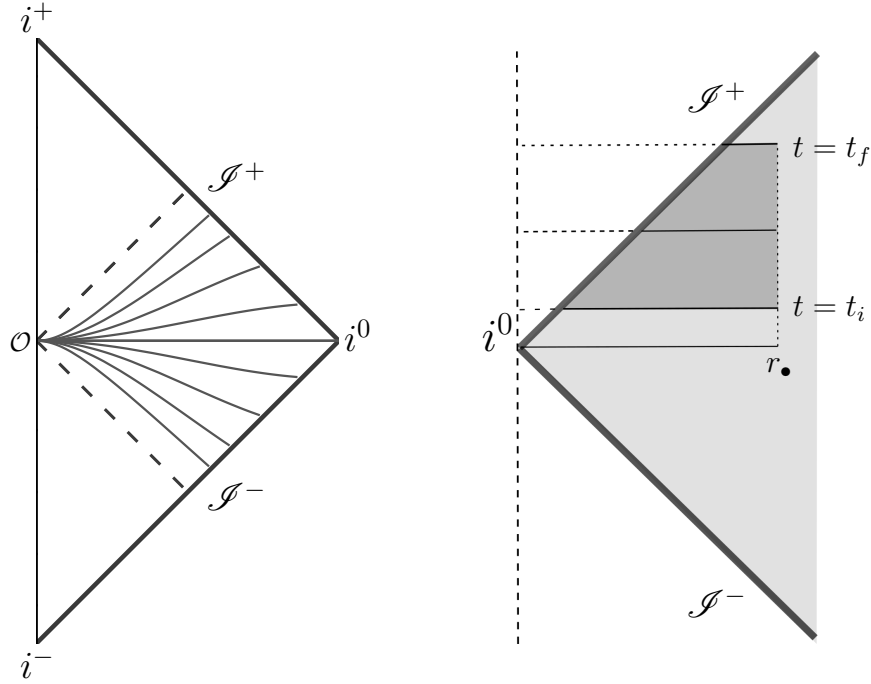


Figure 2: The left panel shows the $t = \text{const}$ surfaces plotted on the Penrose diagram of the Minkowski spacetime. The right panel shows a coordinate diagram of the inversion-Minkowski spacetime where the $t = \text{const}$ surfaces are shown. The numerical evolutions are started at $t = t_i \neq 0$ to avoid i^0 and the grid corresponds to $r \in (0, r_\bullet]$.

4.2 Numerical evolutions

We have implemented the 3+1 decomposed equations described in the previous subsection in coordinates (t, r, θ, ϕ) using the NRPy+ software [45]. NRPy+ is a python infrastructure that allows the input of tensorial expressions in Einstein notation and outputs highly optimised C code that compiles and runs within the same infrastructure. Hence, NRpy+ is well suited for the numerical evolutions performed here, as the system of interest comprises a total of 68 evolved variables in three spatial dimensions, several of which satisfy long differential equations. Despite these challenges, we are able to perform the numerical evolutions in standard desktop computers thanks to the simplicity and efficiency of NRPy+. The code uses the method of lines with a fourth-order Runge-Kutta for time integration. Note that for the inversion-Minkowski spacetime background the slice $t = 0$ intersects i^0 , where the scri-fixing technique discussed in this paper does not work, as mentioned in subsection 3.3, so we are forced to start our simulation at some later time. We choose $t = 0.5$ as the starting time for all our evolutions —see diagram 2. Moreover, since the inversion-Minkowski spatial coordinates (r, θ, ϕ) mimic standard spherical coordinates in physical Minkowski spacetime, we discretise the spatial dimensions employing a staggered grid with equally spaced (N_r, N_θ, N_ϕ) cells in the (r, θ, ϕ) directions and one gridpoint lying exactly at the centre of each cell. This way we avoid the direct evaluation of quantities at the coordinate singularities, corresponding to the z axis. The spatial domain consists of $r \in (0, 40)$, $\theta \in [0, \pi]$ and $\phi \in [0, 2\pi]$. Spatial derivatives are approximated with second-order accurate centred finite differences.

Notice that background quantities appear in the evolution equations, as clearly shown in equations (13). In particular, for the inversion-Minkowski spacetime the background conformal

factor $\dot{\Xi}$ is a time-dependent quantity. For different spacetimes one could consider, several background quantities can have this property. One relevant extension of the present work is the implementation of time-dependent right-hand-sides for the evolved quantities within the NRPy+ infrastructure, which was not available in the first public version of the code. We expect to be able to exploit this tool in future work. As previously mentioned, the inversion-Minkowski space-time background was chosen because of its simplicity, however, it should be emphasised that the (background) location of \mathcal{J}^+ is determined by $\dot{\Xi} = 0$, which corresponds to the points such that $r = t$ (see the given expression in (11)). Hence, as our grid is fixed in the (r, θ, ϕ) coordinates, this implies that as time evolves we have increasing number of gridpoints lying outside of the corresponding physical Minkowski spacetime —see diagram 2. This problem is commonly faced in the numerical evolution of the CEFs, as generically the conformal factor depends on time.

One way to remedy loosing larger parts of the grid into the “unphysical region” of the conformal extension, would be to use a choice of hyperboloidal foliation according to the prescription in [35] for which the background conformal factor is not time dependent. Despite the fact that the scri-fixing through gauge source functions for the linearised CEFs discussed in section 3.3 can accommodate for this possibility, the price to pay is that the background curvature becomes non-zero. This makes the equations more cumbersome to deal with and the background spatial metric is no longer the flat metric that is already incorporated in NRPy+. Although these modifications do not represent a problem at the level of the formulation, incorporating more general backgrounds would involve making further changes to the NRPy+ code. Hence, we have opted to stick to the inversion-Minkowski background for the proof-of-concept numerical evolution presented here and leave other more interesting backgrounds such as the hyperboloidal representation of Minkowski of [35] or the conformal representation of Minkowski, de-Sitter and anti-de Sitter in the Einstein cylinder for future work.

As is standard in NRPy+, we rescale the angular components of the tensorial quantities by the appropriate factor to evolve purely $O(1)$ quantities near the points $r \sin \theta = 0$. This implies that for every covariant θ index we rescale this component by a factor of r and for every ϕ index with a factor $r \sin \theta$. More concretely, if Λ_θ is any tensorial component appearing in the equations of motion we write it as $\Lambda_\theta = r \tilde{\Lambda}_\theta$ and evolve $\tilde{\Lambda}_\theta$. On the contrary, contravariant angular components such as say $\tilde{\Lambda}^\theta$ and $\tilde{\Lambda}^\phi$ are rescaled by r^{-1} and $(r \sin \theta)^{-1}$ respectively. These rescalings provide a better setup to deal with the coordinate singularities, which lie closer to the gridpoints as resolution is increased. We also apply artificial dissipation to all evolved variables to improve convergence and stability at the origin. We do this via fourth order Kreiss-Oliger dissipation with a dissipation parameter $\sigma = 0.02$. Importantly, we increase resolution near the coordinate singularities with a factor in front of the Kreiss-Oliger angular derivatives of tensorial quantities according to the prescription described in the previous paragraph, namely, a $(r \sin \theta)^{-2}$ in front of ∂_ϕ^2 of a rank-2 tensor, etc.

There are two types of numerical boundaries, the so-called *inner* and *outer*. The inner ones correspond to the boundaries of the angular coordinates or the points where $r < 0$. To fill ghost points beyond the boundaries of the angular coordinates we simply input the corresponding value from the gridpoint inside the grid. For the $r < 0$ gridpoints we do so with the appropriate parity conditions that must be satisfied by the different tensorial components. All of this is standard in NRPy+ and is explained in [45]. For the outer boundary we use fourth order extrapolation in all the variables. Note there is no physical motivation for both boundary conditions in r , as the points $r < 0$ are outside of the physical Minkowski spacetime and $r > 40$ corresponds to the finite value of \tilde{r} for which there could be incoming radiation. These facts imply that our numerical solution only represents physically viable scenarios in the future domain of dependence of our initial data. A deeper study on how to include the the whole physical domain —i.e containing the physical origin $\tilde{r} = 0$ — with appropriate boundary conditions will also be addressed in an upcoming work.

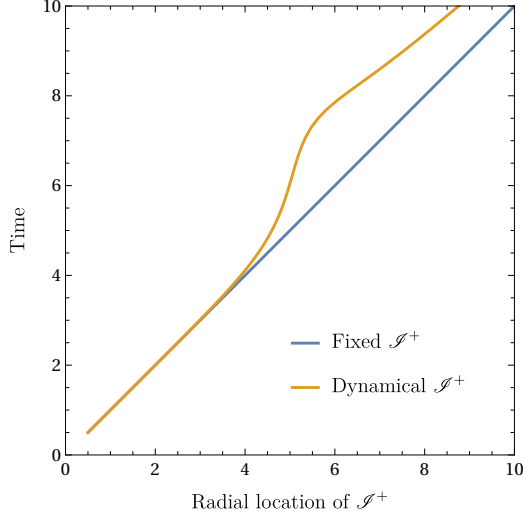


Figure 3: Location of \mathcal{I}^+ as a function of time for both scri-fixing and trivial gauge source functions.

Finally, a comment about initial data is in order. If a solution to equations (13) is to represent a solution to the linearised CEFs we need to solve the linearised version of the CEF-constraints to determine the initial data. This requires a thorough study on how to numerically solve the constraints, which lies out of the scope of the present work. Ultimately, for this proof-of-concept experiment we are concerned with the numerical evolution with the scri-fixing gauge sources, which is independent of the initial data solution. Therefore we test all of our numerical simulations with constraint-violating initial data.

4.2.1 Spherically symmetric evolutions

As a first test, we perform numerical evolutions with spherically symmetric initial data, which implies that the whole evolution remains spherically symmetric. We run our simulations with $N_r = 160$ and $N_\theta = N_\phi = 2$ gridpoints, both for scri-fixing and trivial gauge source functions. Setting two gridpoints in the coordinates that are not being used is a technical requirement of NRPy+. As initial data we set for all the evolved fields:

$$S_{\text{sph}}(r) = A_s r^n e^{-(r^2 - c^2)^2 / 4\sigma^2},$$

where $c = 10$ for all variables, $A_s = 0$ for $\delta\Xi(0, r)$, $A_s = 10^{-2}$ and $n = 0$ for $\delta g_{nn}(0, r) = \delta s(0, r)$, $A_s = 10^{-2}$ and $n = 2$ for $\delta\Phi_{nn}(0, r) = \delta\Phi_{rr}(0, r) = \delta E_{rr}(0, r) = \delta B_{rr}(0, r)$ and $A_s = 10^{-2}$ and $n = 3$ for $\delta\Phi_{nr}(0, r) = \delta g_{nr}(0, r)$. Notice that the condition $\delta\Phi_{nn}(0, r) = \delta\Phi_{rr}(0, r)$ ensures that $\delta\Phi_{ab}$ is trace-free. Finally we set $A_s = -10^{-2}/2$ and $n = 4$ for $\delta E_{\theta\theta} = \delta E_{\phi\phi} / \sin^2 \theta = \delta B_{\theta\theta} = \delta B_{\phi\phi} / \sin^2 \theta$ to guarantee δE_{ij} and δB_{ij} are trace-free. We set zero initial data for the remaining components and for all reduction variables.

In figure 3 we plot the location of \mathcal{I}^+ as a function of time for our two sets of gauge source functions. In the scri-fixing case, this plot coincides with the $r = t$ line as $\delta\Xi = 0$, whereas the other case does not, as expected. The curve representing the location of \mathcal{I}^+ in the trivial gauge sources case (labelled as “dynamical” in figure 3) is found through a root-finding method at each timestep. Hence, it can, in general, become non-smooth even for smooth initial data if $\delta\Xi$ becomes non-monotonic as a function of r .

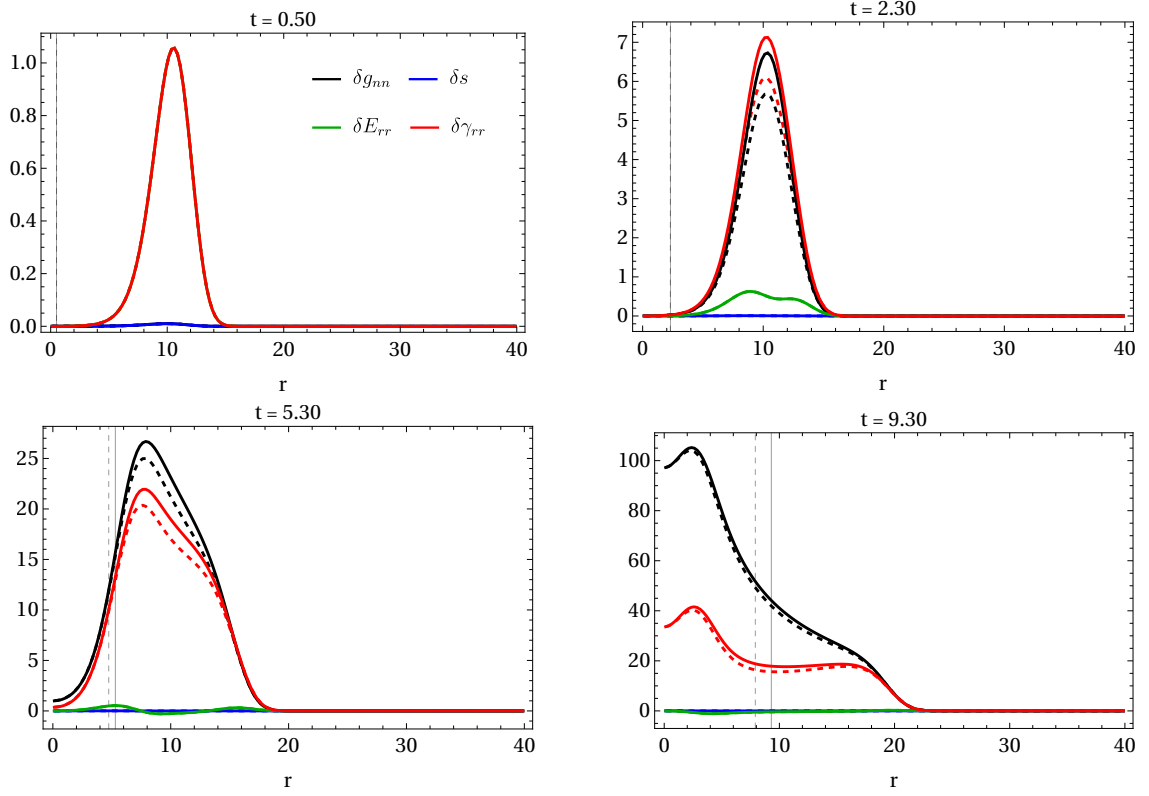


Figure 4: Snapshots of evolved fields for both scri-fixing and trivial gauge source functions.

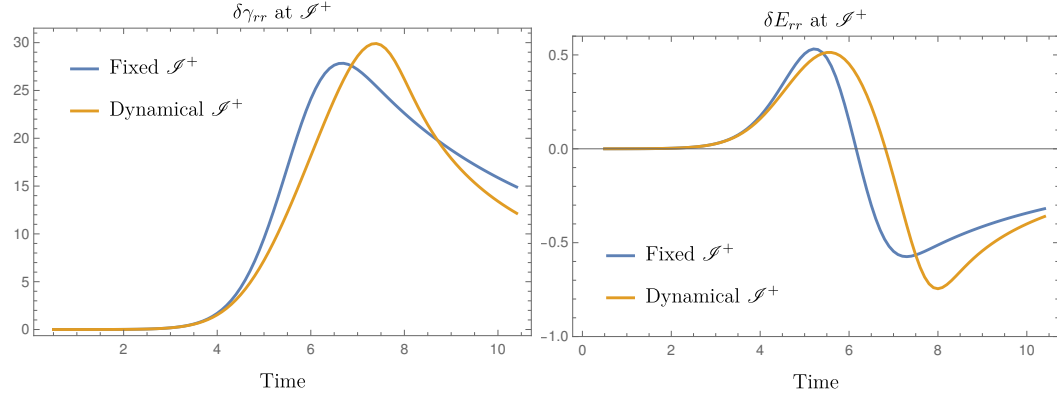


Figure 5: Example of evolved fields evaluated at the points plotted in figure 3 for both sets of gauge sources.

In figure 4 we plot snapshots of some of the evolved fields both with scri-fixing gauge sources (solid lines) and trivial gauge sources (dashed lines). Additionally, we plot the location of \mathcal{S}^+ at each time with a vertical line, also with a solid or dashed line depending on each case. Note that the location of \mathcal{S}^+ at each time is found by solving the equation $\dot{\Xi} + \delta\Xi = 0$. Since $\delta\Xi = 0$ for scri-fixing (up to numerical error) and $\delta\Xi \neq 0$ for trivial gauge sources, the location of \mathcal{S}^+ differs between these two cases in the same way as shown in figure 3 above. Moreover, since the scri-fixing gauge sources enter the right-hand-side of evolution equations of the metric perturbations, both δg_{nn} and $\delta \gamma_{rr}$ differ as functions of code coordinates during the evolution.

On the other hand, coordinate gauge sources do not appear in the equations of motion for δs , δE_{ij} or δB_{ij} and they are decoupled from the rest. Therefore, these fields coincide in the evolution in the code's coordinates for the two sets of gauge sources we test, as shown in figure 4. Finally, having found the location of \mathcal{S}^+ as a function of time we can evaluate the fields directly at those values by interpolating the numerically evolved fields. Examples with the two sets of gauge sources are plotted in figure 5. Note that, despite δE_{ij} , δB_{ij} and δs being identical as functions of the coordinates, their evaluation at \mathcal{S}^+ differs between the two sets of gauge sources because the location of \mathcal{S}^+ is different. This “ambiguity” ultimately comes from the decoupling of the Bianchi-sector from the metric-sector of the linearised equations and from interpreting the location of \mathcal{S}^+ as either the locus points of $\dot{\Xi} = 0$ or $\Xi := \dot{\Xi} + \delta\Xi = 0$. In the non-linear case there is no such decoupling and hence no ambiguity. Therefore, the scri-fixing gauge sources in the linear case can be thought as a way to remove this ambiguity by ensuring that $\delta\Xi = 0$.

4.2.2 Axially symmetric evolutions

We then proceed with simulations in axial symmetry, for both sets of gauge sources. As our first simulation we take $N_r = 80$, $N_\theta = 50$ and $N_\phi = 2$ gridpoints. Similarly to the spherically-symmetric case we set as initial data for all variables

$$\begin{aligned} S_{\text{ax}}(r) &= A_a r^n R(r) Y_{20}(\theta, \phi) \\ R(r) &= [(4c^2 r^2 + 8cr^3 + 4r^4 - 2c\sigma^2 r - 4\sigma^2 r^2 - \sigma^4)/\sigma^4 \\ &\quad (-4c^2 r^2 + 8cr^3 - 4r^4 - 2c\sigma^2 r + 4\sigma^2 r^2 + \sigma^4) e^{4cr/\sigma^2}/\sigma^4] \frac{e^{-(r+c)^2/\sigma^2}}{r} \end{aligned}$$

where Y_{20} is the $l = 2$, $m = 0$ spherical harmonic and $c = 8$ in this case. This initial data is smooth at the origin, with the expression inspired by the d'Alembert partial-wave solution to the wave equation [46]. We make identical choices for n and $A_a = A_s/2$ for exactly the same fields as in the spherically symmetric case. In figure 6 we plot snapshots of the location of \mathcal{S}^+ in the yz plane. Note that, once again, in the scri-fixing case the plots coincide with the $r = t$ curve, drawing a circle in our coordinates, and in the trivial gauge sources case they are deformed, as expected.

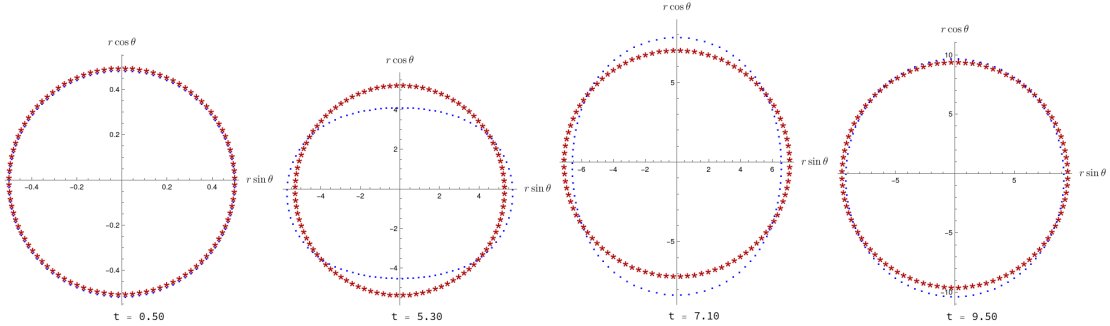


Figure 6: Snapshots of the location of \mathcal{S}^+ .

In Figures 7 - 8 we plot snapshots of $\delta\gamma_{rr}$ and δE_{rr} . In these figures, the first row corresponds to evolutions with trivial gauge sources while the second row correspond to the case of scri-fixing gauge sources. The colours blue and orange in these plots represent the physical and unphysical region of the conformal extension respectively. The location of \mathcal{S}^+ corresponds to the boundary between these two, which is again found by solving the equation $\dot{\Xi} + \delta\Xi = 0$ for every angle. Analogous to the spherically-symmetric case, the evolution of $\delta\gamma_{rr}$ as function of code coordinates differs between the different sets of gauge sources, contrary to the evolution of δE_{rr} , which is unaffected. This feature can be seen comparing first and second rows, respectively. For

the chosen data, the difference is, nevertheless, small. If one considers a larger amplitude A_a for the initial data the difference is much more noticeable, however the routine used to find the location of \mathcal{I} has difficulties to find the roots giving non-smooth features in Figure 6.

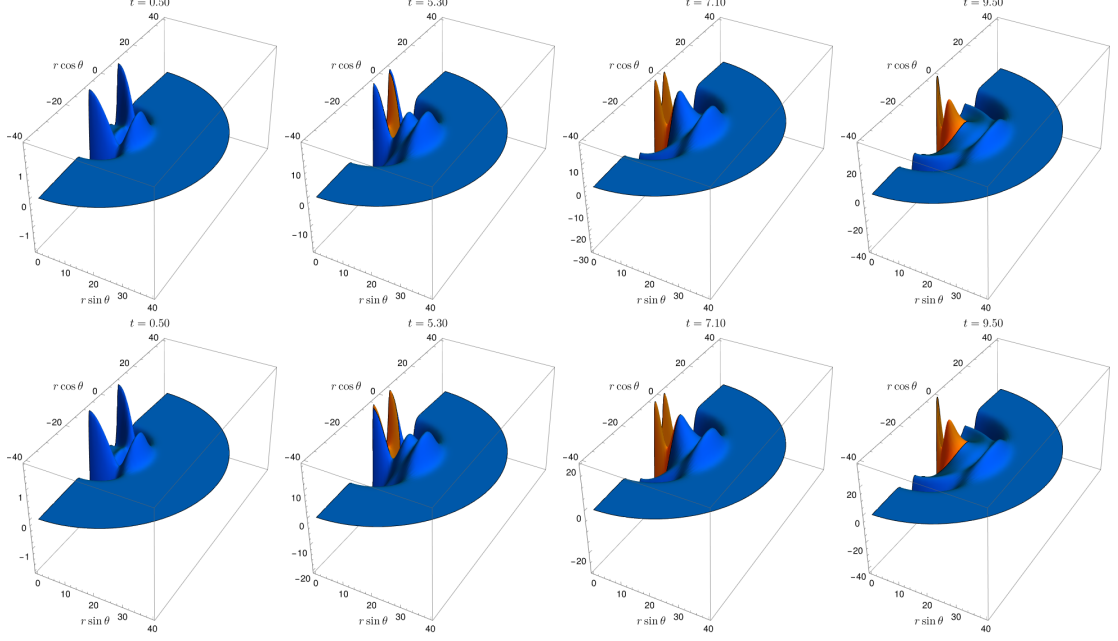


Figure 7: $\delta\gamma_{rr}$ snapshots with trivial gauge sources (top) and scri-fixing gauge sources (bottom).

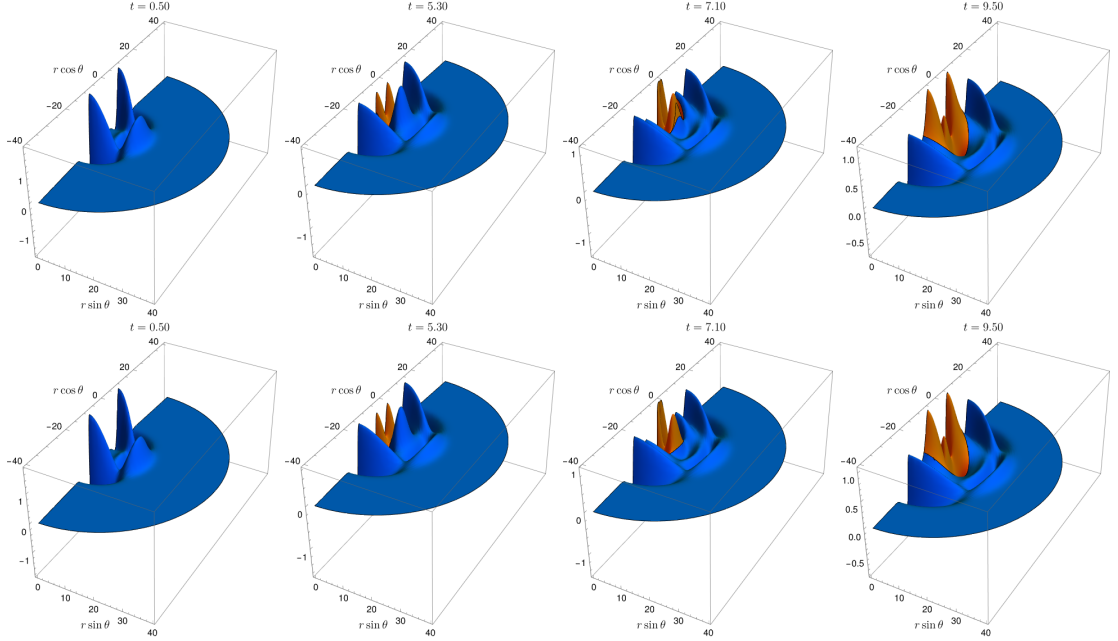


Figure 8: δE_{rr} snapshots with trivial gauge sources (top) and scri-fixing gauge sources (bottom).

With the location of \mathcal{I}^+ in terms of our coordinates we are able to extract the value of the evolved fields in these points. In figure 9 we plot again $\delta\gamma_{rr}$ and δE_{rr} to illustrate this. The fields now depend also on the angular coordinate θ , so we denote the amplitude of the fields in

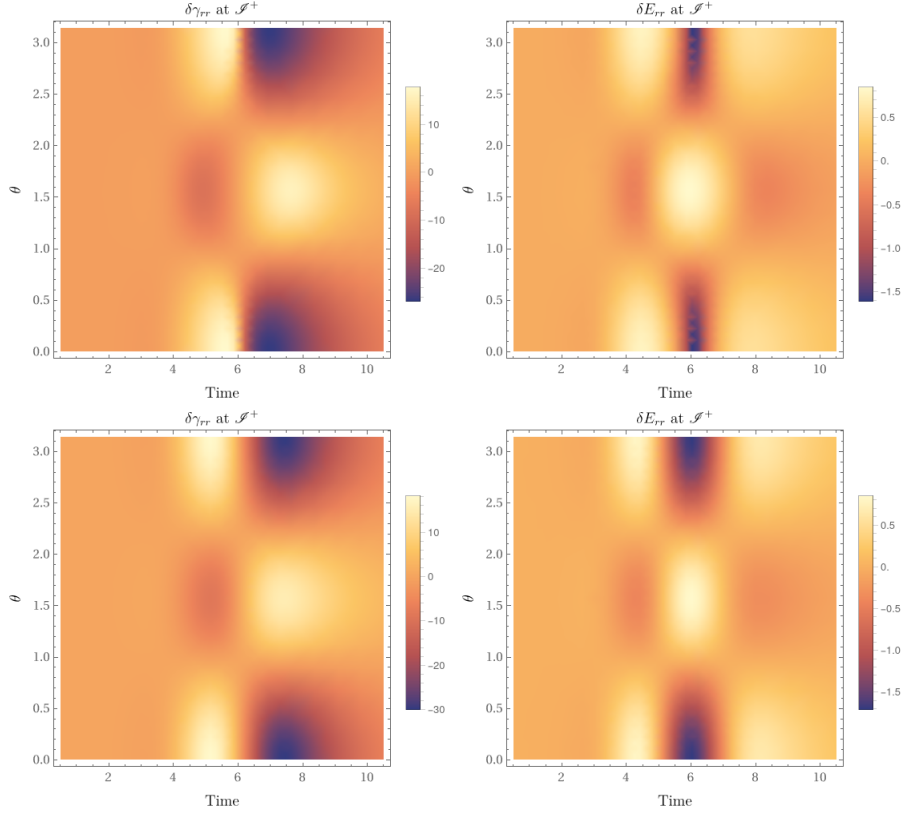


Figure 9: Trivial gauge sources (top) and scri-fixing gauge sources (bottom).

colour. Note that, despite δE_{rr} being the same function of (t, r) for both sets of gauge sources, its value at \mathcal{S}^+ differs between the two cases because of the difference in the location of \mathcal{S}^+ , as discussed previously. We then proceed to do a self-convergence test of our simulations by tripling N_r and N_θ twice, starting with $N_r = 80$ and $N_\theta = 16$ and computing the difference between adjacent resolutions in the overlapping gridpoints. This is done for both sets of gauge sources. We then compute the L^2 norm of these two differences of all evolution quantities and compute the corresponding convergence order according to the formula

$$\text{Convergence order} = \log_3 \left(\frac{\sqrt{\sum_{i=1}^{N_r} \sum_{j=1}^{N_\theta} (X_{low,i,j} - X_{med,i,j})^2}}{\sqrt{\sum_{i=1}^{N_r} \sum_{j=1}^{N_\theta} (X_{med,i,j} - X_{high,i,j})^2}} \right) \quad (17)$$

with $X_{low/med/high,i,j}$ denoting each of the evolution variables for the low, medium and high resolutions at point i, j . In figure 10 we plot the convergence order as a function of time. Note that, since we use second-order finite differences, ideal convergence would correspond to the number 2. This is compatible with figure 10, meaning the numerical errors are converging away at the expected rate in the limit of infinite resolution.

5 Conclusions and perspectives

In this article we perform numerical evolutions of a linearised version of the second order metric formulation of the CEFs introduced in [33] —see also [32]—, which has the advantage that it resembles more closely the standard formulation of the Einstein field equations used in Numerical

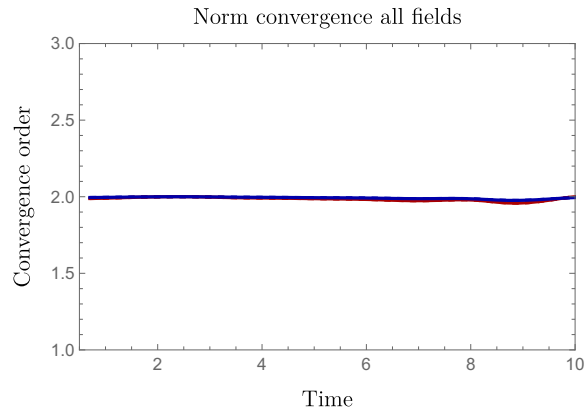


Figure 10: Norm convergence for both cases. The red line corresponds to the case of trivial gauge source functions and the blue line to scri-fixing gauge source functions.

Relativity than other hyperbolic reductions of the CEFs. Although the construction of initial data is not addressed, the numerical evolutions performed here serve as a proof-of-concept calculation to illustrate numerically the scri-fixing strategy through gauge source functions for the linear case discussed in [1]. The main advantage of this scri-fixing strategy is that it allows to choose the conformal factor in an essentially ad-hoc way without solving any differential equation. If this strategy is indeed generalisable to the non-linear case then it would allow to employ in the CEFs the same gauges (same conformal factor) used in the formally singular hyperboloidal approach [14, 16] but with formally regular equations. To test these ideas at the linear level, we have used the linear equations of [1] in the simplest possible background: the inversion-Minkowski spacetime. Notice that similar evolutions can be performed in other backgrounds at the expense of more complicated expressions. In particular, one could use the Einstein cylinder to perform evolutions of the Minkowski, de-Sitter and anti-de Sitter spacetimes. Naturally, in all these cases the equation for the perturbation of the rescaled Weyl tensor decouples from the rest. This observation has been exploited in other explorations of the spin-2 equation representing the linearisation of the Bianchi sector of the CEFs [47, 48, 49]. However, the philosophy in this article is that the complete system is to be evolved as relevant physical information is also encoded in the metric perturbation.

Acknowledgements

We are grateful to Zach Etienne and Leonardo Rosa Werneck for answering questions regarding the implementation of time-dependent equations in NRPy. We have benefited from conversations with David Hilditch. C. Peterson thanks the financial support to IST-ID through Project No. UIDB/00099/2020. E. Gasperín holds an FCT (Portugal) investigator grant 2020.03845.CEECIND and held an FCT Exploratory Research Project 2022.01390.PTD during the time this research was conducted. A. Vañó Viñuales thanks FCT for financial support through Project No. UIDB/00099/2020 and for the FCT funding with DOI 10.54499/DL57/2016/CP1384/CT0090.

References

- [1] Justin Feng and Edgar Gasperín. Linearised conformal einstein field equations. *Classical and Quantum Gravity*, 40(17):175001, July 2023.

- [2] C Denson Hill and Pawel Nurowski. How the green light was given for gravitational wave search, 2016.
- [3] Lydia Bieri, David Garfinkle, and Nicolas Yunes. Gravitational waves and their mathematics, 2017.
- [4] H. Bondi, M. G. J. van der Burg, and A. W. K. Metzner. Gravitational waves in general relativity. vii. waves from axi-symmetric isolated systems. *Proceedings of the Royal Society of London. Series A, Mathematical and Physical Sciences*, 269(1336):21–52, 1962.
- [5] R. K. : Sachs and Hermann Bondi. Gravitational waves in general relativity viii. waves in asymptotically flat space-time. *Proceedings of the Royal Society of London. Series A. Mathematical and Physical Sciences*, 270(1340):103–126, 1962.
- [6] Ezra Newman and Roger Penrose. An approach to gravitational radiation by a method of spin coefficients. *Journal of Mathematical Physics*, 3(3):566–578, 1962.
- [7] Robert P. Geroch. Asymptotic structure of space-time. In F. Paul Esposito and Louis Witten, editors, *Asymptotic Structure of Space-Time*, pages 1–105, Plenum Press, New York, 1977. Springer US.
- [8] Abhay Ashtekar. Radiative degrees of freedom of the gravitational field in exact general relativity. *Journal of Mathematical Physics*, 22(12):2885–2895, 12 1981.
- [9] Francisco Fernández-Álvarez. News tensor on null hypersurfaces, 2024.
- [10] A. Ashtekar. Geometry and Physics of Null Infinity. *ArXiv e-prints*, September 2014.
- [11] Roger Penrose. Conformal treatment of infinity. In C. DeWitt and B. DeWitt, editors, *Relativity, Groups, and Topology (Les Houches, France, 1964)*, pages 565–584. Gordon and Breach, New York, 1964.
- [12] Anil Zenginoglu. Hyperboloidal evolution with the Einstein equations. *Class. Quant. Grav.*, 25:195025, 2008.
- [13] Alex Vañó-Viñuales. *Free evolution of the hyperboloidal initial value problem in spherical symmetry*. PhD thesis, U. Iles Balears, Palma, 2015.
- [14] Alex Vañó-Viñuales. Spherically symmetric black hole spacetimes on hyperboloidal slices. *Frontiers in Applied Mathematics and Statistics*, 9, August 2023.
- [15] David Hilditch, Enno Harms, Marcus Bugner, Hannes Rüter, and Bernd Brügmann. The evolution of hyperboloidal data with the dual foliation formalism: Mathematical analysis and wave equation tests. *Class. Quant. Grav.*, 35(5):055003, 2018.
- [16] Christian Peterson, Shalabh Gautam, Alex Vañó Viñuales, and David Hilditch. Spherical evolution of the generalized harmonic gauge formulation of general relativity on compactified hyperboloidal slices, 2024.
- [17] H. Friedrich. On the Regular and the Asymptotic Characteristic Initial Value Problem for Einstein’s Vacuum Field Equations. *Proc. R. Soc. Lond. A*, 375(1761):169–184, March 1981.
- [18] Juan-Antonio Valiente-Kroon. *Conformal Methods in General Relativity*. Cambridge University Press, Cambridge, 2016.
- [19] Helmut Friedrich. Spin-2 fields on minkowski space near spacelike and null infinity. *Classical and Quantum Gravity*, 20(1):101–117, dec 2002.

- [20] Edgar Gasperín and Juan A. Valiente Kroon. Perturbations of the asymptotic region of the schwarzschild–de sitter spacetime. *Annales Henri Poincaré*, pages 1–73, 2017.
- [21] Marica Minucci and Juan A Valiente Kroon. On the non-linear stability of the cosmological region of the schwarzschild-de sitter spacetime. *Classical and Quantum Gravity*, 40(14):145005, June 2023.
- [22] Georgios Doulis and Jörg Frauendiener. Global simulations of minkowski spacetime including spacelike infinity. *Phys. Rev. D*, 95:024035, Jan 2017.
- [23] Peter Hübner. A scheme to numerically evolve data for the conformal Einstein equation. *Class. Quantum Grav.*, 16:2823–2843, 1999.
- [24] Peter Hübner. From now to timelike infinity on a finite grid. *Class. Quantum Grav.*, 18:1871–1884, 2001.
- [25] J Frauendiener and C Stevens. The non-linear perturbation of a black hole by gravitational waves. i. the bondi–sachs mass loss. *Classical and Quantum Gravity*, 38(19):194002, September 2021.
- [26] Jörg Frauendiener, Alex Goodenbour, and Chris Stevens. The non-linear perturbation of a black hole by gravitational waves. iii. newman-penrose constants, 2023.
- [27] Marcus Ansorg and Rodrigo Panosso Macedo. Spectral decomposition of black-hole perturbations on hyperboloidal slices. *Phys. Rev.*, D93(12):124016, 2016.
- [28] Anil Zenginoğlu, Darío Núñez, and Sascha Husa. Gravitational perturbations of schwarzschild spacetime at null infinity and the hyperboloidal initial value problem. *Classical and Quantum Gravity*, 26(3):035009, January 2009.
- [29] José Luis Jaramillo, Rodrigo Panosso Macedo, and Lamis Al Sheikh. Pseudospectrum and Black Hole Quasinormal Mode Instability. *Phys. Rev. X*, 11(3):031003, 2021.
- [30] Rodrigo Panosso Macedo and Anil Zenginoglu. Hyperboloidal approach to quasinormal modes, 2024.
- [31] Rodrigo Panosso Macedo, Patrick Bourg, Adam Pound, and Samuel D. Upton. Multidomain spectral method for self-force calculations. *Physical Review D*, 110(8), October 2024.
- [32] Diego A. Carranza, Adem E. Hursit, and Juan A. Valiente Kroon. Conformal wave equations for the einstein-tracefree matter system. *General Relativity and Gravitation*, 51(7), jul 2019.
- [33] T.-T. Paetz. Conformally covariant systems of wave equations and their equivalence to Einstein’s field equations. *Ann. Henri Poincaré*, 16:2059, 2013.
- [34] Alex Vañó Viñuales and Tiago Valente. Height-function-based 4D reference metrics for hyperboloidal evolution. *General Relativity and Gravitation*, 56(135), 11 2024.
- [35] Anil Zenginoğlu. Hyperboloidal foliations and scri-fixing. *Classical and Quantum Gravity*, 25(14):145002, jun 2008.
- [36] J. Frauendiener. Numerical treatment of the hyperboloidal initial value problem for the vacuum Einstein equations. II. the evolution equations. *Phys. Rev. D*, 58:064003, 1998.
- [37] J. Stewart. *Advanced general relativity*. Cambridge University Press, 1991.
- [38] Edgar Gasperín and David Hilditch. The Weak Null Condition in Free-evolution Schemes for Numerical Relativity: Dual Foliation GHG with Constraint Damping. *Class. Quant. Grav.*, 36(19):195016, 2019.

- [39] J Frauendiener and C Stevens. The non-linear perturbation of a black hole by gravitational waves. ii. quasinormal modes and the compactification problem. *Classical and Quantum Gravity*, 40(12):125006, May 2023.
- [40] A García-Parrado Gómez-Lobo, E Gasperín, and J A Valiente Kroon. Conformal geodesics in spherically symmetric vacuum spacetimes with cosmological constant. *Classical and Quantum Gravity*, 35(4):045002, January 2018.
- [41] Helmut Friedrich. Conformal geodesics on vacuum space-times. *Communications in Mathematical Physics*, 235(3):513–543, April 2003.
- [42] David Hilditch, Enno Harms, Marcus Bugner, Hannes Rüter, and Bernd Brügmann. The evolution of hyperboloidal data with the dual foliation formalism: Mathematical analysis and wave equation tests. *Class. Quant. Grav.*, 35(5):055003, 2018.
- [43] Alex Vañó-Viñuales, Sascha Husa, and David Hilditch. Spherical symmetry as a test case for unconstrained hyperboloidal evolution. *Class. Quant. Grav.*, 32(17):175010, 2015.
- [44] Rodrigo Panosso Macedo. Hyperboloidal approach for static spherically symmetric space-times: a didactical introduction and applications in black-hole physics. *Philosophical Transactions of the Royal Society A: Mathematical, Physical and Engineering Sciences*, 382(2267), January 2024.
- [45] Ian Ruchlin, Zachariah B. Etienne, and Thomas W. Baumgarte. SENR/NRPy+: Numerical Relativity in Singular Curvilinear Coordinate Systems. *Phys. Rev.*, D97(6):064036, 2018.
- [46] Isabel Suárez Fernández, Rodrigo Vicente, and David Hilditch. Semilinear wave model for critical collapse. *Physical Review D*, 103(4), February 2021.
- [47] Florian Beyer, Georgios Doulis, Jörg Frauendiener, and Ben Whale. Linearized gravitational waves near space-like and null infinity, 2013.
- [48] Rodrigo P Macedo and Juan A Valiente Kroon. Spectral methods for the spin-2 equation near the cylinder at spatial infinity. *Classical and Quantum Gravity*, 35(12):125007, May 2018.
- [49] J. A. Valiente Kroon. Polyhomogeneous expansions close to null and spatial infinity. In J. Frauendiener and H. Friedrich, editors, *The Conformal Structure of Spacetimes: Geometry, Numerics, Analysis*, Lecture Notes in Physics, page 135. Springer, 2002.